NUMERICAL STUDY OF DIRECTIONAL EHD CONDUCTION DRIVEN FLOW DISTRIBUTION CONTROL IN SMALL SCALES IN THE PRESENCE OF EXTERNAL PRESSURE LOADS

Michal Talmor & Jamal Seyed-Yagoobi
Multi-Scale Heat Transfer Laboratory
Dept. of Mechanical Engineering
Worcester Polytechnic Institute, Worcester MA
phone: (1) 508-831-5236
e-mail: mtalmor@wpi.edu, jyagoobi@wpi.edu

Recent advances in miniaturization have enabled modern day electronics to continue to uphold Moore's Law, which predicts that the component densities of electronic devices will be doubled every two years, exponentially increasing their computational capabilities. However, one of the greatest challenges facing further development of advanced MEMS and NEMS electronic devices is the thermal management and removal of heat generated by such a high component density. Traditional high performance fluidic thermal systems use mechanical means to control the flow, but these are not easily miniaturized and require comparatively high power and constant maintenance to operate continuously. Therefore, new technological solutions for thermal management at small scales, such as EHD conduction pumping, need to be utilized to enable the next generation of miniaturized electronics to be developed. In EHD conduction, a strong electric field is applied via asymmetric electrodes submerged in a dielectric fluid. The electric field enhances the chemical dissociation of electrolytic impurities within the fluid into ionic species, which then migrate to form heterocharge layers over each electrode. The subsequent abundance of asymmetrically distributed space charge causes a net Coulomb force to be applied on the fluid, generating motion in the desired direction. EHD conduction pumps have no moving parts, draw very little power due to very low current consumption, and have simple, flexible designs that can be easily miniaturized to the micro-scale. This study numerically investigates utilizing EHD conduction pumps to control the distribution of flow between parallel small-scale channels, using different pumping orientations and accounting for different downstream pressure loads. The results are compared with available experimental data gathered for EHD conduction driven flow distribution control of single and two phase flows.

I. Introduction

Electrohydrodynamic conduction pumping uses the interaction between a strong applied electric field and dissociated electrolyte impurities within a dielectric working fluid. Electrolyte impurities are present in all dielectric fluids, and undergo a reversible chemical process of dissociate into ionic species and recombination back into neutral molecules. In the absence of a strong electric field, the equilibrium reaction rates for the dissociation and recombination reactions are equal to each other, and the overall fluid is considered electroneutral [1]. This reversible reaction as denoted as,

$$AB \underset{\text{Recombination}}{\overset{\text{Dissociation}}{\rightleftharpoons}} A^+ + B^- \tag{1}$$

When a strong electric field is applied between submerged electrodes in the working fluid, the rate of the dissociation reaction exceeds that of the recombination reaction, leading to an excess of ionic charges. These charges migrate toward the oppositely charged electrodes due to the electric field, and drag the working fluid's molecules in their solvation sheath along [2]. A new equilibrium is then formed, in which the dissociated ions retain their charges within thin layers that form over each electrode, and recombine into neutral species after transiting across these layers and encountering oppositely charged species. These regions of space charge are called heterocharge layers [3]. The overall fluid still remains electroneutral, but the heterocharge layers represent an accumulation of local space charges, which is acted upon by Coulomb forces due to the electric field. This generates opposing local volumetric forces that act upon the working fluid. The dimensions of the heterocharge layers, and the resulting force magnitudes, depend on the electrode geometry. Under the assumption of equal ionic mobilities for the positive and negative ions, if electrodes with equal wetted areas are used the opposing Coulomb forces will balance each other out and only flow circulation would occur. If an asymmetrical electrode design is used instead, a net force and a net flow will be generated in the direction of the electrode with the largest wetted surface area [4]. A general schematic of the EHD conduction mechanism, for flat electrodes flush with the fluid channel, is shown in Fig. 1.

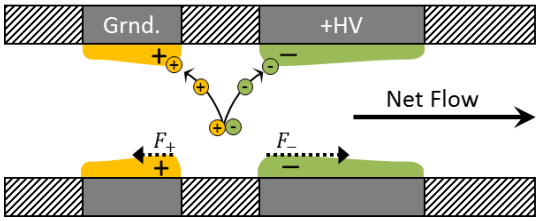

Fig. 1. Schematic of EHD Conduction Mechanism

EHD conduction has been investigated theoretically and numerically by several researchers over the last few decades. Based on fundamental work on dissociation and conduction of charges in a dielectric medium done by Pontiga and Castellanos [5], Atten & Seyed-Yagoobi [6] first presented the mathematical model for the EHD conduction phenomenon and established the key nondimensional parameters related to EHD

conduction pumping performance. Yazdani & Seyed-Yagoobi [7] performed the first numerical simulations using this nondimensional model for the EHD conduction mechanism, providing the first simulated profiles for the heterocharge layers, for a simple geometry. Further numerical studies by Yazdani & Seyed-Yagoobi [8] investigated the effect of the ratio of the positive and negative ionic mobilities on the pumping performance of EHD conduction, since in realistic applications equal ionic mobilities are not guaranteed. Gharraei et al. [9] performed similar simulations on a dimensional model and compared the results to experimental data, showing a good prediction of the effect of changes to mobility using true mobility data, and investigating the relationship between this effect and the effect of the electrode asymmetry ratio on the pumping performance. Mahmoudi et al. [101 showed that these numerical models could also be used for the prediction of pressure generation performance of an EHD conduction pump. Studies of the effect of charge convection due to the generated flow on the heterocharge layer were conducted numerically by Feng & Seyed-Yagoobi [11], and were experimentally observed by Patel & Seyed-Yagoobi [12].

These numerical studies have verified the general validity of the mathematical model as a predictive tool of EHD conduction performance, but have focused on simulating only a single pair of electrodes using periodic boundary conditions to simulate the remainder of the electrode pairs, and have thus far not investigated the effect of an externally applied loads on the EHD conduction mechanism or pumping performance.

EHD conduction driven flow distribution control studies have thus far focused on experimental efforts. Feng & Seyed-Yagoobi [13, 14], for example, experimentally investigated EHD conduction driven flow distribution control of single and two-phase flows in macro-scale. Yang et al. [15, 16] experimentally investigated flow distribution control in single and two-phase flows in meso-scale, and compared the results with rudimentary numerical simulations based solely on performance data that was previously gathered for the EHD conduction pump used. These studies showed that EHD conduction pumps are an effective method of controlling flow distribution between parallel branches in multiple size scales, and can be used to recover from maldistribution of flow or a sudden dryout condition. Sinnamon [17] proposed a structural panel with distributive channels, and an embedded EHD conduction driven thermal control system to control the flow in these channels. However, to the author's knowledge, no numerical simulations of the fully coupled electrostatics, flow and charge conservation equations of the EHD conduction mechanism have been performed for EHD conduction driven flow distribution control applications.

The purpose of the work presented here is therefore to utilize the mathematical models for the fully coupled EHD conduction equations in order to perform numerical studies of EHD conduction driven flow distribution between parallel channels in small scales, using multiple electrode pairs and different pumping orientation configurations, in the presence and absence of externally applied pressure loads. In addition, this study will provide fundamental explanations for different pumping behaviors based on the morphology of the simulated heterocharge layer formation process under different flow and external pressure load conditions. The model used is dimensional and utilizes published data for R-123 as the working fluid properties.

II. Mathematical Model

The EHD conduction pumping mechanism relies on three core physics models that must be coupled and solved together to arrive at a simulation solution. These three models describe the electrical field and charge density, the fluid flow, and the charge conservation within the working fluid. The electrical field is described by the familiar electrostatics Poisson Equation,

$$\nabla \cdot \bar{E} = \nabla^2 \Phi = -\frac{\rho_e}{\varepsilon} = -\frac{(p_e - n_e)}{\varepsilon} \tag{2}$$

where $\bar{E}$ is the electric field, Φ is the electric potential, ε is the electric permittivity, and ρ_e is the total charge density as defined by the ionic charge densities p_e and n_e. The fluid flow is described by the standard mass continuity and Navier-Stokes equations for the conservation of the rate of change of momentum,

$$\nabla \cdot \bar{u} = 0 \tag{3}$$

$$(\bar{u} \cdot \nabla)\bar{u} = \nabla \cdot [-\bar{P} + \mu(\nabla \bar{u})] + F \tag{4}$$

where $\bar{u}$ is the fluid velocity, $\bar{P}$ is the pressure gradient, and μ is the fluid viscosity. These equations assume that the working fluid is incompressible and has constant properties. The final term in Equation 4 is the Coulomb force, which couples the electrostatics and fluid flow models together,

$$F = (p_e - n_e)E \tag{5}$$

The charge concentration conservation is often described by the conservation of current density for the positive and negative ionic currents,

$$\nabla \cdot \bar{J}_{\pm} = \left[-D_i \nabla \rho_{e,\pm} - z_i b \rho_{e,\pm} \nabla \Phi\right] + \bar{u} \cdot \nabla \rho_{e,\pm} = R_i \tag{6}$$

where $\bar{J}$ is the current density, D_i is the diffusion coefficient for the charge carrier, b is the electric mobility for the charge carrier, z_i is the charge number, and $\rho_{e,\pm}$ is the charge density for the charge carrier. For this numerical study, however, an equivalent description was used, based on the Nernst-Planck equation for conservation of concentration of charged species,

$$\nabla \cdot [-D_i \nabla c_i - z_i b c_i \nabla \Phi] + \bar{u} \cdot \nabla c_i = R_i \tag{7}$$

The c_i term stand for the concentrations of negative and positive charges, n and p, respectively, which are solved for separately.

The concentration and charge density are simply related via the unit charge, e_0,

$$p_e = e_0 p \qquad , \qquad n_e = e_0 n \tag{8}$$

The ionic mobility term is considered to be a constant, such that the mobilities of each ionic species are the same. The diffusion coefficient for the working fluid is obtained from the Stokes-Einstein relation for charged particles [18],

$$D = bk_B T \tag{9}$$

The last term in Equation 7 represents the reaction rates for the generation of charges. This term is the same for both concentrations,

$$R_i = k_D n_0 - k_R np \tag{10}$$

which results in the following expression,

$$R_i = \frac{2bN_A e_0 (n_0)^2}{\varepsilon}\left(F(\omega_e) - \frac{pn}{(n_0)^2}\right) \tag{11}$$

where N_A is Avogadro's constant, and n_0 is the equilibrium concentration of the ionic species, in the absence of the strong electric field,

$$n_0 = p|_{E=0} = n|_{E=0} \tag{12}$$

In the above equation, $F(\omega_e)$ is known as the Onsager field enhancement function, which represents the increase in the dissociation rate [19]. This function is defined using the Onsager parameter, ω_e,

$$F(\omega_e) = \frac{I_1(4\omega_e)}{2\omega_e} \tag{13}$$

$$\omega_e = \sqrt{\frac{(e_0)^3 E}{16\pi\varepsilon k_B^2 T^2}} \tag{14}$$

These equations were solved using the COMSOL Multiphysics 5.0 software, using the Electrostatics, Laminar Flow, and Transport of Diluted Species model components to represent the three physics models described here.

III. Boundary Conditions

To complete the simulation model, the set of boundary conditions given in Table 1 was provided to the software.

Table 1: Model Boundary Conditions

Location	Conditions
High voltage electrode wetted surface	$\Phi = V_0 \quad , \quad n = 0 \quad , \quad \frac{\partial p}{\partial \hat{n}} = 0$
Ground electrode wetted surface	$\Phi = 0 \quad , \quad p = 0 \quad , \quad \frac{\partial n}{\partial \hat{n}} = 0$
Fluid channel walls	$\frac{\partial \Phi}{\partial \hat{n}} = 0 \quad , \quad u = 0 \quad , \quad \frac{\partial n}{\partial \hat{n}} = \frac{\partial p}{\partial \hat{n}} = 0$
Outer wall surrounding the fluid channel	$\Phi = 0$
Fluid channel inlet	$n = p = n_0 \quad , \quad u = u_0$
Fluid channel outlet	$\frac{\partial n}{\partial \hat{n}} = \frac{\partial p}{\partial \hat{n}} = 0 \quad , \quad P = P_{out}$

Noting that $\hat{n}$ is a surface normal coordinate and V_0 is the applied electric potential on the high voltage electrode. For the fluid model, P_{out} is the outlet pressure. For the inlet, either an incoming flow velocity, u_0, or an inlet pressure, P_{in}, was provided, depending on the case being examined. These cases and their corresponding inlet and outlet boundary conditions are outlined in Table 2.

Table 2: Inlet/Outlet Boundary Condition Cases

Case Type	Inlet Boundary Condition	Outlet Boundary Condition
No external loads, flow distribution or maldistribution	Velocity corresponding to desired flow rate	Zero pressure
Two-phase load downstream	Velocity corresponding to desired flow rate	Applied two-phase pressure load

IV. Simulation Domain & Cases

The simulation domain was comprised of two sub-domains. The primary domain was used for the fluid flow modeling, and was comprised of a joint inlet, joint outlet, and a split into two channels in the middle. The secondary domain was used only for the electrostatics modeling of the electric field in the pump's enclosing walls. These two domains are shown schematically in Figure 2. The top and bottom branches had a height of 1mm, while the fluid inlet and outlet had a height of 2mm to minimize their impact on the pressure drop opposing the EHD pump's operation. The lengths of the inlet and outlet portions were chosen to ensure that developing flow effects from an inadequate entrance length would not affect the flow in the branches. For the initial maldistribution cases, a constriction was introduced in either the top or bottom branch, representing a valve. The dimensions of the constrictions were variable, so that different maldistributions for the same inlet flow could be studied.

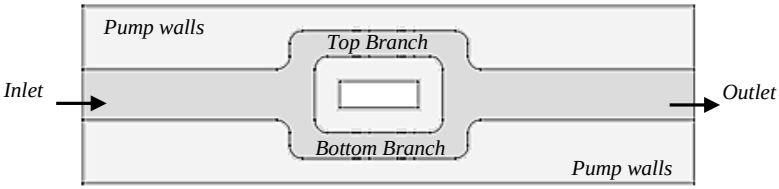

Fig. 2. Overview of the simulation domain

Both top and bottom branches shown in this figure contained EHD conduction pumps comprised of two electrode pairs, as shown in Figure 3. The electrodes were modeled as being flush with the flow channel surface, as a facsimile of flush ring electrodes in a tube with a circular cross-section. The dimensions of the electrodes were chosen based on a pump previously studied by Patel & Yagoobi [20], and are provided in Table 3.

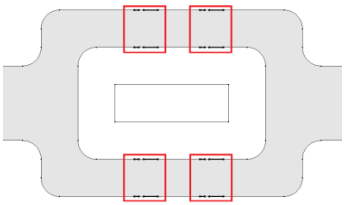

Fig. 3. Electrode pair locations

Table 3: EHD Pump Dimensions

Dimension	Size
High voltage electrode	0.381 mm
Ground electrode	0.127 mm
Space between electrodes	0.127 mm
Space between electrode pairs	1.524 mm

The mesh for this domain was comprised of 48,810 elements with an average element quality of 0.67. The mesh was optimized to provide results at a resolution of 1μm in the relevant areas of charge transport and flow boundary layers, while utilizing coarser elements in less critical areas to keep the computational time and memory consumption down. The mesh for the secondary wall domain, for instance, only contains 9,200 elements. This optimization process was done incrementally, to minimize any errors related to the mesh size and resolution.

TABLE 4: STUDY CASES

Case Type	Pump Orientation	Flow Rates [mL/min[	Outlet Excess Pressures [Pa]
Flow redistribution	Forward	1 – 10	0
	Reverse	1 – 10	0
Maldistribution recovery	Forward	1 – 5	0
	Reverse	1 – 5	0
Two-phase load recovery	Forward	1 – 10	1 – 15
	Reverse	1 – 10	1 – 15

The different cases that were studied are summarized in Table 4. For the downstream two-phase pressure load simulations, the values for the loads were chosen based on pressure drop calculations from published correlations for flow boiling frictional pressure drops in mini and micro-channels [21], based on the Martinelli parameter, X, which describes the ratio between the pressure drop of a single liquid phase flow through a channel and the pressure drop of a single vapor phase flow through the same channel,

$$X^2 = \left(\frac{dp}{dz}\right)_{liquid} \Big/ \left(\frac{dp}{dz}\right)_{vapor} \tag{15}$$

$$C = 12(1 - e^{-319D_h}) \tag{16}$$

$$\Phi_L^2 = 1 + \frac{C}{X} + \frac{1}{X^2} \tag{17}$$

$$\frac{dp}{dz} = \Phi_L^2 \left(\frac{dp}{dz}\right)_{liquid} \tag{18}$$

$$\Delta P_{evap} = \frac{dp}{dz} L \tag{19}$$

In these equations, Φ_L^2 is called the two-phase multiplier, used to estimate the pressure drop of a two-phase flow from the pressure drop of a single phase flow. C is a diameter correction constant for the hydraulic diameter, D_h. The specific form shown in Equation 16 was chosen for an assumed laminar liquid phase flow, which is what is expected from the EHD conduction driven flow, and a turbulent vapor phase flow from boiling. The pressure drop per unit distance is obtained via Equation 18 and, assuming a simple length of tube, can be multiplied by the channel length the two-phase media is expected to flow through before full condensation occurs, L, as is done in Equation 19. For this study, the calculated pressure drop values for flow boiling occurring at the outlet of the simulation domain were in the range of 20 – 35 Pa.

Conversely, a calculation for the pressure generation required upstream of the inlet to maintain the desired flow rates was done using the Darcy-Weisbach equation,

$$\Delta P_{upstream} = \frac{8 f_D}{(\pi)^2} \frac{\dot{m}^2}{\rho D_h^5} \tag{20}$$

where $\dot{m}$ is the mass flow rate, ρ is the fluid density, and f_D is the Darcy friction factor. The friction factor is defined for laminar flow through a circular pipe using the Reynolds number, Re,

$$\mathrm{f_D} = \frac{64}{Re} = 64 \frac{\mu}{\rho u D_h} \tag{21}$$

From the above equations, the pressure generation needed from the upstream flow rate source in order to maintain the maximum flow rates shown in Table 4 was 20 Pa. Thus, for the upstream evaporation cases, the inlet pressure was used as the zero-level reference point, and the outlet pressure condition is the excess pressure load imposed by the evaporation process.

V. Results and Discussion

The simulation cases were run in COMSOL Multiphysics 5.0. The physical model equations (2)-(4) and (7), as well as the boundary conditions shown in Table 1, were represented in the software using the Electrostatics, Laminar Flow, and Transport of Diluted Species modules. The solver allowed error was set to 10^{-5} to ensure accurate results within a reasonable time frame. Post-processing of the results was done via the built-in Matlab Livelink feature. As the model equations are dimensional, the fluid properties shown in Table 5 were used for the working fluid in the simulation. These properties correspond to those of HCFC-123, a common refrigerant. The following sub-sections describe the results of the different cases described in Table 4.

Table 5: Working Fluid Properties [22]

Density [kg/m^3]	**Viscosity [Pa·s]**	**Dielectric Strength**	**Electric Conductivity [S/m]**
1470	4.357×10^{-4}	4.825	2.7×10^{-8}

A. Flow redistribution – Forward & Reverse Orientation

The first cases considered in this study were for redistribution of an initially equally distributed flow in the parallel channels. Two configurations were considered for these cases – forward pumping orientation and reverse pumping orientation. In the former, the pump is oriented such that its flow generation is directed from the inlet of the domain toward the outlet, in line with the main flow. In the latter, the pump is oriented in the reverse direction, in opposition to the main flow. In both configurations only one branch's pump was activated, while the other branch's pump remained inactive. Figure 4 shows the results of the simulations for both configurations for the lowest input flow rate level considered, 1 mL/min. In this figure, we see that the ability to diverge the flow is roughly the same between the two configurations. Both are able to initiate the divergence at 100V, and both cause the flow in one of the branches to stagnate at 500V and fully reverse direction at 1500V. The primary difference is that for the forward configuration, the flow reversal occurs in the inactive branch, while in the reverse configuration the flow reversal occurs in the activated branch. Therefore for this low flow rate case, it can be concluded that the forces generated by each configuration are the same.

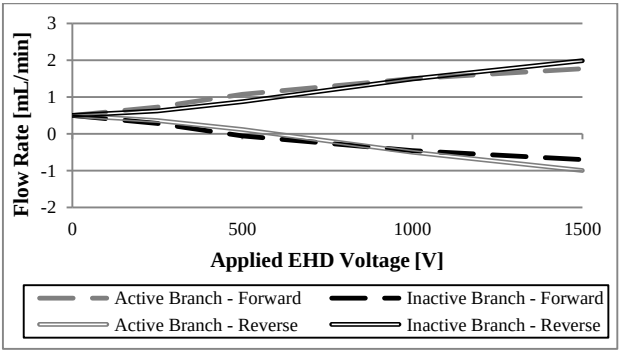

Fig. 4. Forward vs. reverse orientation redistribution – 1 mL/min supply flow rate

However, this was not the case for higher flow rates. Figure 5 shows the simulation results for an initially equally distributed inlet flow rate of 4 mL/min. In this figure, we see that the forward orientation is unable to diverge the flow as effectively as the reverse orientation. The point of initiation of divergence for the forward orientation has been delayed to 400V, while it remained at 100V for the reverse orientation. In addition, the pump in the reverse orientation was still able to cause the flow to stagnate in one branch, at 1400V, and begin reversing at 1500V, unlike the pump in the forward orientation. Subsequently, the final total flow rate divergence of the two configurations was vastly different: a 1mL/min difference between the branches for the forward orientation, versus a 2mL/min difference for the reverse orientation. This trend continued in the remaining simulation cases, where the initiation of divergence continued being delayed for the forward orientation as the inlet flow rate was increased, while remaining unchanged for the reverse orientation, and the final divergence at 1500V for the reverse orientation continued to be much larger than that of the for the forward orientation. This increase in performance is explained in the final sub-section, as part of the discussion of the simulation results for the heterocharge layer formation process.

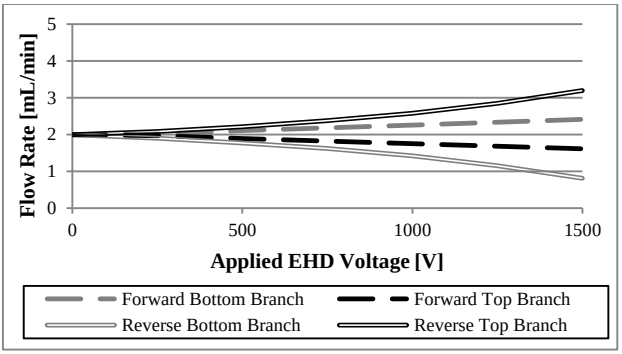

Fig. 5. Forward vs. reverse orientation redistribution – 4 mL/min supply flow rate

B. Maldistribution Recovery – Forward & Reverse Orientation

The next cases to be considered in this study were for recovery from a maldistribution condition, where the flow is initially unequally distributed between the two branches, and the activation of the EHD conduction pump in one of the branches is intended to equalize the distribution. In this set the forward and reverse configurations were also studied, with only one branch pump being activated. For the forward configuration, the inactive branch had the high flow rate, so activation of the pump increased the flow rate in the active branch. For the reverse configuration, the active branch start with the high flow rate, and activation of the pump diverted the flow into the inactive branch. Figure 6 shows the results for an initial maldistribution of 1mL/min inlet flow rate into 0.3mL/min and 0.7mL/min. In this figure, the performance of the two configurations is similar. As shown, the forward configuration achieves equalization of the flow rates at 400V, versus 500V for the reverse configuration. The other notable difference is that the reverse configuration was able to achieve flow stagnation and some flow reversal in the active branch with further application of voltage, while the forward configuration was only able to achieve flow stagnation in the inactive branch at the maximum voltage.

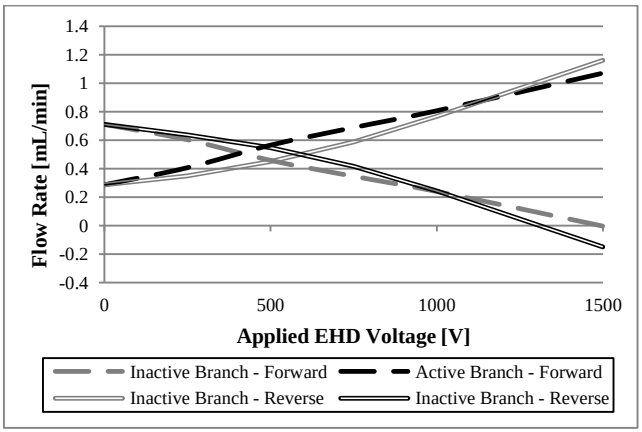

Fig. 6. Forward vs. reverse orientation maldistribution recovery – 1 mL/min supply flow rate

Figure 7 shows the results for 2mL/min distributed into 0.6mL/min vs. 1.4mL/min. In this figure, both the forward and reverse configurations achieve flow equalization at the same voltage level of 1000V. Before this voltage level, the performance of the two configurations appears very similar. However, after the point of flow equalization, the reverse configuration is once again better able to diverge the flow, as was shown in the previous sub-section.

Figure 8 shows a similar case, with a greater initial separation of the flow. In this figure, the 2mL/min inlet flow is distributed into 0.5mL/min and 1.5mL/min. As shown, the performance of both configurations is similar up to 1200V. However, the reverse configuration is able to achieve flow equalization sooner, at 1400V, as opposed to the forward configuration, that only achieved this at 1500V. In both cases, even a small change in the initial maldistribution greatly affected the performance of both EHD conduction pump configurations.

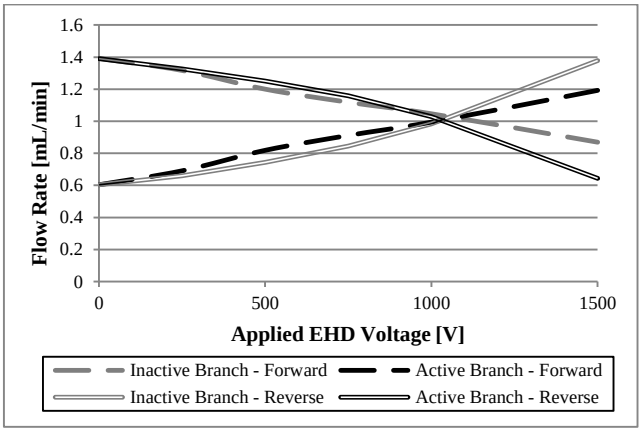

Fig. 7. Forward vs. reverse orientation maldistribution recovery – 2 mL/min supply flow rate

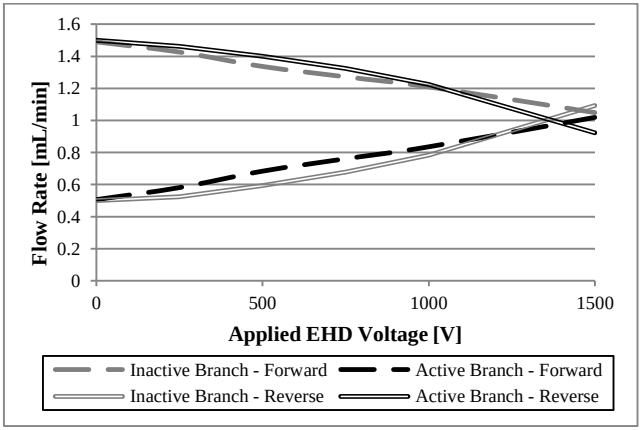

Fig. 8. Forward vs. reverse orientation maldistribution recovery – wider initial separation of 2 mL/min

The last case presented in this sub-section is for maldistribution of a 4mL/min inlet flow into 1.25mL/min and 2.75mL/min, as shown in Figure 9. This case represents the limit at which the reverse pumping configuration was able to equalize the flow at the maximum voltage level. As shown, the forward configuration was not able to significantly affect the flow distribution, or provide meaningful recovery from the maldistribution, even at the maximum applied voltage.

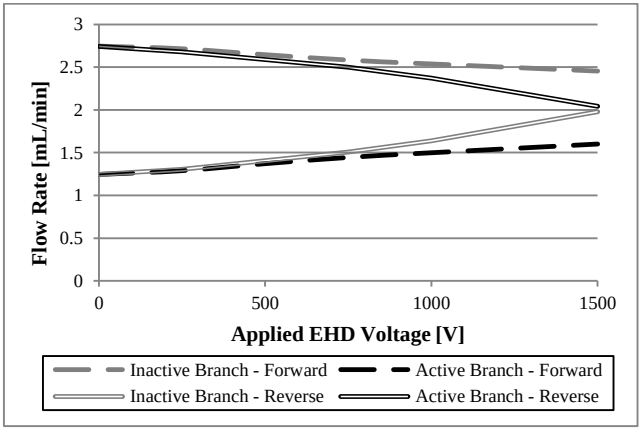

Fig. 9. Forward vs. reverse orientation maldistribution recovery – 4 mL/min supply flow rate

C. Evaporation Load at Outlet

The purpose of the cases shown in this sub-section was to test the potential capability of EHD driven flow distribution control to overcome a potential dryout condition. In these simulations, a dryout condition is assumed to occur when the pressure load applied at the outlet of the domain is sufficient to cause flow stagnation or reversal in the domain branches. This represents the case where the vapor from an evaporation process occurring downstream of the outlet will not be propelled to move toward the condenser section by the main flow, since the pressure load from the evaporation is too high for the main flow to overcome. If the vapor cannot be evacuated from the evaporator section by the main flow, dryout would soon follow.

Figures 10 and 11 show the flow rates in each of the branches for different evaporation pressure loads at the outlet, using either the forward or reverse pumping configurations, with the EHD conduction pump activated at its maximum voltage. The outlet pressure loads are given in these figures as the total calculated loads from evaporation, rather than the differential boundary conditions used in the simulation. It should be noted that for these simulations the bottom branch was always the one whose pump was activated, while the top branch was always inactive.

Therefore, Figure 10 shows that the reverse configuration bolstered the flow in the inactive branch so it could withstand the pressure load and maintain a positive flow rate up to 32.5 Pa. Conversely, since the forward configuration was draining flow away from the inactive branch, it was only able to withstand the pressure load up to 25 Pa.

However, figure 11 shows that in order to allow for the inactive branch in the reverse configuration to maintain a positive flow, the flow in the active branch was entirely reversed for all the pressure loads. In contrast, the flow in the active branch in the forward configuration was never reversed. From these results it can concluded that, while the reverse configuration outperforms the forward configuration in single-phase flow distribution control, it is less suitable for two phase flow distribution control and dryout recovery it. Nevertheless, adding an EHD conduction pump in the reverse orientation may allow a flow distribution system to boost the flow in a different branch, especially if the activated branch is not expected to have two-phase flow.

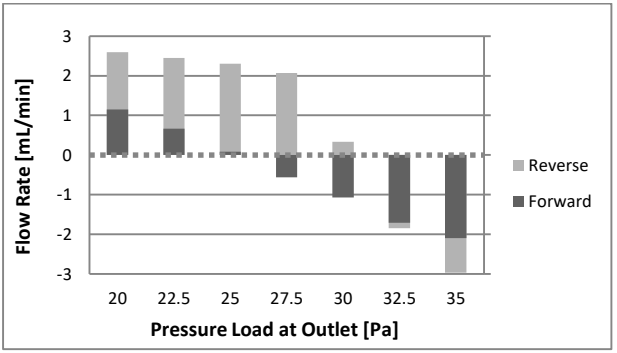

Fig. 10. Orientations - top branch flow rate vs. two-phase load, bottom branch pump at constant 1500 V

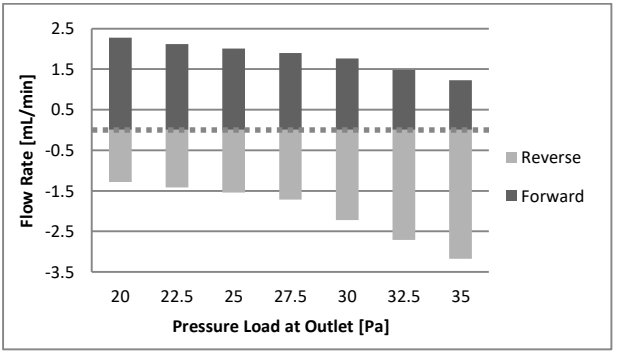

Fig. 11. Orientations - bottom branch flow rate vs. two-phase load, bottom branch pump at constant 1500 V

Additional cases involving activation of both branch pumps to overcome the pressure load from a downstream evaporation process also considered. However, based on the previous results, only the forward pumping configuration was tested. In these cases, the pump in the bottom branch was always activated at its maximum applied voltage, but the voltage was varied 0-1500V in the top branch pump. Figure 12 shows some of the results for these cases. In this figure, the flow rate in the top branch is being equalized with the flow rate in the bottom branch as the applied voltage is increased, much like the maldistribution recovery cases. Unlike the forward configuration's maldistribution recovery behavior in the absence of this external load, the flow rates are always equalized, regardless of the magnitude of the load. The difference between the loads is the final achievable flow rates in each

branch, with higher loads corresponding to lower overall flow rates as expected. The results in Figure 12 also show that with this sort of setup, while the bottom branch never experienced dryout due to the presence of the fully activated pump, the top branch is forced to recover from dryout for loads greater than 25 Pa, and is successful in doing so. Therefore, in the presence of a potential downstream load, originating from an evaporation process or any other phenomenon, the forward configuration is highly effective in maintaining the flow and recovering from a condition that would cause flow reversal in one of the branches.

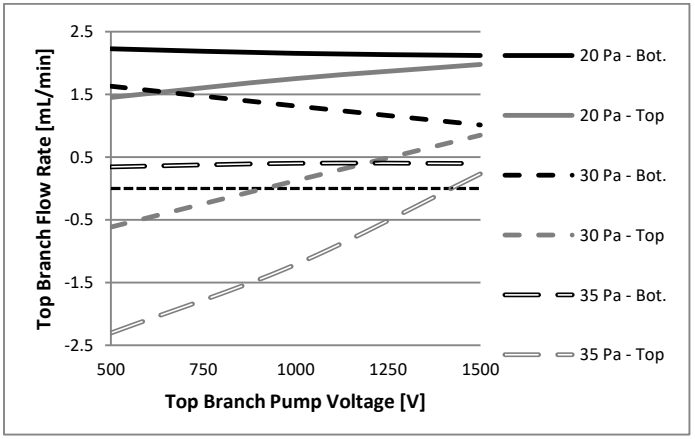

Fig. 12. Forward orientation only – top branch flow rates vs. voltage, bottom branch pump at constant 1500 V

A. Heterocharge Layer Morphology

To explain the behaviors shown in the previous sub-sections, the shape and dimensions of the heterocharge layes over the electrodes were investigated as well. Figure 13 shows a characteristic set of heterocharge layers over the two electrode pairs of a forward configuration pump activated at its maximum applied voltage, under different inlet supply flow rates. At the maximum voltage the layers are at their maximum thickness, and comparisons between their relative sizes can be made more easily than at lower voltages. The boundaries of the layers are defined as 10% of the total charge density and are shown as a black or white outline in the figure. The flow in Figure 13 is directed from left to right, and the effect of increasing the flow velocity can be readily seen.

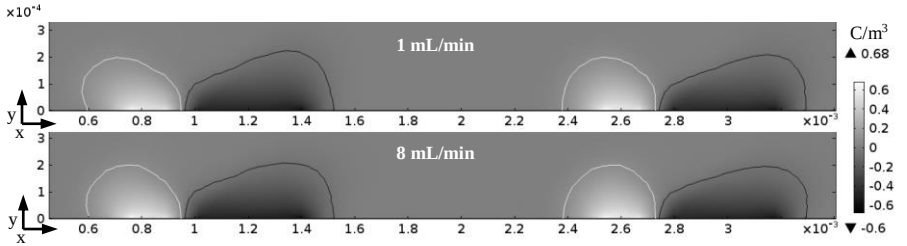

Fig. 13. Heterocharge layers over a forward pump for a supplied flow of 1mL/min (top) and 8mL/min (bottom)

For the low flow rates, the positive charge layer over the ground electrode of the first pair of the pump is relatively long in the x direction and flat in the y direction, while at the higher flow rates this layer is shorter in the x direction and taller in the y direction. While slightly more difficult to see, the negative charge layer over the high voltage electrodes in the pump's first pair is shorter at the higher flow rate than at the lower flow rate. The same trend is seen for the second pair of the pump, but with an added effect from the additional flow rate generated by the first pair. Therefore, the second pair's positive charge layers are always taller in the y direction than the first pair's positive layers, and the negative charge layers of the second pair are always shorter than the ones for the first pair.

These changes may seem minute, but they correspond to large changes in the applied Coulomb forces and subsequent pumping performance. Since the pressure generation of EHD conduction pumps is directly related to the difference between the dimensions of the positive and negative heterocharge layers, the layers thicknesses in the vertical direction were carefully measured and compared. The results for this comparison are shown in Figures 14 and 15, for the first and second electrode pairs respectively, and for both the forward and reverse pumping configurations. It should be noted that while the layers differ in the horizontal direction as well, those differences are much smaller than the ones in the vertical direction and are therefore not shown in this paper.

Figure 14 shows that for the reverse configurations, increasing the supplied flow rate to the inlet of the domain increases the difference between the positive and negative charge layers for the first pair, since the negative charge layer over the high voltage electrode significantly increases in size, while the positive charge layer over the ground electrode becomes moderately smaller. The opposite effect is seen for the forward pumping configuration, since the negative layer decreases in size and the positive layer increases in size with higher supply flow rates. This serves to explain why the reverse configuration seems to outperform the forward configuration in redistributing the flow or recovering from maldistribution. It also serves to explain why the forward configuration is better used when there are applied loads at the outlet, which create a flow that opposes the main flow.

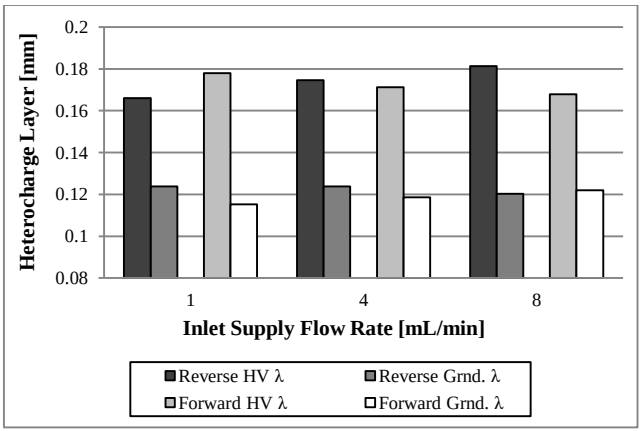

Fig. 14. Heterocharge layers over a forward pump for a supplied flow of 1mL/min (top) and 8mL/min (bottom)

Figure 15 shows the same sort of layer thickness measurements for the second electrode pairs of the forward and reversed configuration pumps. Here we see that the difference in sizes between the positive and negative charge layers for the reverse configurations is greater for the second pair than it is for the first pair, and continues increasing with higher supply flow rates. Once again, the reverse trend is seen for the forward configuration, where the thickness difference between the layers reducing further with higher supply flow rates, and being overall lower than in the first pair. This serves to explain the effect of diminishing returns for adding electrode pairs that has seen in experiments for forward configuration EHD conduction pumps. While the addition of pairs increases the overall pump performance, the erosion of the heterocharge layers of subsequent pairs by the flow generation of previous pairs leads to there being a point where additional pairs are no longer of benefit to the pump. These results also show that the performance of EHD conduction pumps is vastly improved in the presence of an opposing flow. In such a configuration, instead of a diminishing return on the pumping performance, a significant incremental gain is obtained with the addition of electrode pairs. It should, however, be noted that these effects would not be apparent in the case of static pressure generation, where flow cannot develop and modify the heterocharge layer thicknesses over any of the EHD conduction pump electrodes.

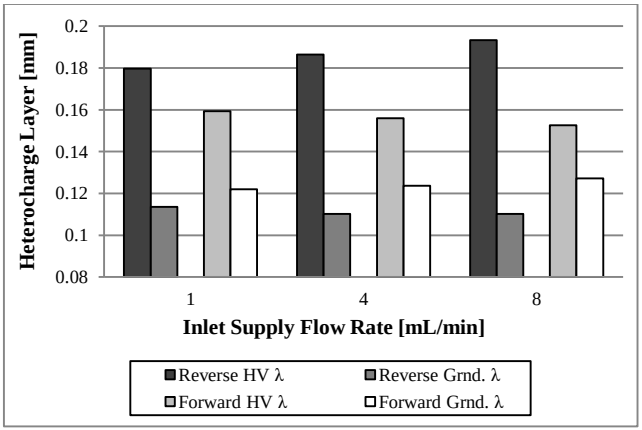

Fig. 15. Heterocharge layers over a forward pump for a supplied flow of 1mL/min (top) and 8mL/min (bottom)

VI. Conclusion

Numerical simulations of EHD conduction driven flow distribution control, using the fully coupled EHD conduction equations, were performed on a small-scale domain. Of the two configurations studied, forward and reverse pumping configurations, the reverse configuration has overall better performance. The forward configuration's performance is only equal or better than the reverse configuration at very low inlet supply flow rates. This trend is seen both for flow redistribution cases and for maldistribution recovery cases, and is explained by the heterocharge layer morphology.

Nevertheless, in the cases simulating a downstream pressure load, such as from the vapor phase in a downstream evaporator section, the forward configuration was the only

viable method of preventing both branches from experiencing flow reversal, and therefore dryout.

The heterocharge layer formation for multiple electrode pairs was also studied and quantified, showing that the trend of charge growth on subsequent electrode pairs beyond the first is greatly affected by the application of external loads – in the form of an externally supplied inlet flow rate, or opposing flow. Such potential loads therefore play a critical role in the overall performance of multi-pair EHD conduction pumps and must be accounted for in the design of such devices in future thermal systems.

ACKNOWLEDGEMENTS

This project was financially supported by the NASA Headquarters Micro-Gravity Fluid Physics Program. The first author's work was sponsored by a NASA Space Technology Research Fellowship.

REFERENCES

[1] R. M. Fuoss, "Ionic Association. III. The Euilibrium between Ion Pairs and Free Ions", *Journal of the American Chemical Society*, vol. 80.19, 1958, p. 5059.

[2] A. I. Zhakin, "Solvation Effects in Liquid Dielectrics", *Surface Engineering and Applied Electrochemistry*, vol. 51.6, 2015, p. 540.

[3] J. P. Gosse, "Electric Conduction in Dielectrics", *The Liquid State and Its Electrical Properties, NATO ASI Series*, vol. 193, 1988, p. 503.

[4] J. Seyed-Yagoobi, "Electrohydrodynamic pumping of dielectric liquids," *Journal of Electrostatics*, vol. 63, 2005, p. 861.

[5] F. Pontiga and A. Castellanos, "Electrical Conduction of Electrolyte Solutions in Nonpolar Liquids", *IEEE Transactions on Industry Applications*, vol. 32.4, 1996, p. 816.

[6] P. Atten, J. Seyed-Yagoobi, "Electrohydro-dynamically induced dielectric liquid flow through pure conduction in point/plane geometry", *Transactions on Dielectrics and Electrical Insulation*, vol. 10, 2003, p. 27.

[7] M. Yazdani, J. Seyed-Yagoobi, "Electrically induced dielectric liquid film flow based on electric conduction phenomenon," *IEEE Transactions on Dielectrics and Electrical Insulation*, vol. 16.3, 2009, p. 768.

[8] M. Yazdani, J. Seyed-Yagoobi, "Effect of Charge Mobility on Dielectric Liquid Flow Driven by EHD Conduction Phenomenon", *Journal of Electrostatics*, vol. 72.4, 2014, p. 285.

[9] R. Gharraei, et al. "Experimental investigation of electrohydrodynamic conduction pumping of various liquids film using flush electrodes." *Journal of Electrostatics*, vol. 69.1, 2011, pp. 43-53.

[10] S. R. Mahmoudi, K. Adamiak and G.S.P. Castle, "Prediction of the Static Pressure Generation for an Electrohydrodynamic Conduction Pump", *presented at the 17th IEEE International Conference on Dielectric Liquids*, Trondheim, Norway, 2011.

[11] Y. Feng & J. Seyed-Yagoobi, "Electrical charge transport and energy conversion with fluid flow during electrohydrodynamic conduction pumping", *Journal of Physics of Fluids*, vol. 19.5, 2007, p. 5710.

[12] V. K. Patel, J. Seyed-Yagoobi, "A Mesoscale Electrohydrodynamic Driven Two-Phase Flow Heat Transport Device in Circular Geometry and In-Tube Boiling Heat Transfer Coefficient Under Low Mass Flux", *Journal of Heat Transfer*, vol. 137.4, 2015, p. 41504.

[13] Y. Feng and J. Seyed-Yagoobi, , "Control of Liquid Flow Distribution Utilizing EHD Conduction Pumping Mechanism", *IEEE Transactions on Industry Applications*, vol. 42.2, 2006, pp. 369-377.

[14] Y. Feng & J. Seyed-Yagoobi, "Control of adiabatic two-phase dielectric fluid flow distribution with EHD conduction pumping", *Journal of electrostatics*, vol. 64.7, 2006, pp. 621-627.

[15] 15 L. Yang, M. Talmor, B. C. Shaw, K. S. Minchev, C. Jiang, J. Seyed-Yagoobi, "Flow distribution control in meso scale via electrohydrodynamic conduction pumping", *IEEE Transactions on Industry Applications*, vol. 53.2, 2017, pp. 1431-1438.

[16] L. Yang, M. Talmor, J. Seyed-Yagoobi, "Flow Distribution Control Between Two Parallel Meso-Scale Evaporators With Electrohydrodynamic Conduction Pumping", *presented at the ASME 2016 International Mechanical Engineering Congress and Exposition*, Phoenix, AZ,, 2016.

[17] S. Sinnamon, "Coolant distribution control in satellite structural panels using electrohydrodynamic conduction pumping." PhD dissertation, Department of Mechanical Engineering, University of New Mexico, Albuquerque, NM, 2012.
[18] P. H. Rieger, "Electrochemistry", 1st ed., Champan & Hall, 1994
[19] L. Onsager, “Deviations from Ohm's law in weak electrolytes”, *Journal of Chemical Physics*, vol 9, p. 599, 1934.
[20] V. K. Patel, F. Robinson and J. Seyed-Yagoobi, “Terrestrial and Microgravity Experimental Study of Microscale Heat-Transport Device Driven by Electrohydrodynamic Conduction Pumping”, *IEEE Transactions on Industry Applications*, vol. 49, 2013, pp. 2397-2401.
[21] S. Kandlikar, S. Garimella, D. Li, S. Colin, M. R. King, "Heat transfer and fluid flow in minichannels and microchannels", Elsevier, 2005.
[22] J. E. Bryan, "An experimental study of ion-drag pumping in a vertical axisymmetric configuration," Ph.D. dissertation, Department of Mechanical Engineering, Texas A&M University, College Station, TX, 1990.